THE JOURNAL OF PHYSICAL CHEMISTRY C
A JOURNAL OF THE AMERICAN CHEMICAL SOCIETY
pubs.acs.org/JPCC
Article

Precise Control of Nanoscale Cu Etching via Gas-Phase Oxidation and Chemical Complexation

Published as part of The Journal of Physical Chemistry virtual special issue "Emily A. Carter Festschrift".

Ryan Sheil,[⊥] J. Mark P. Martirez,[⊥] Xia Sang, Emily A. Carter,* and Jane P. Chang*

Cite This: *J. Phys. Chem. C* 2021, 125, 1819−1832

Read Online

ACCESS | Metrics & More | Article Recommendations | Supporting Information

ABSTRACT: We present a cyclic process for selective and anisotropic atomic layer etching of copper: an oxygen plasma modulates the depth and directionality of the oxidized layer, while formic acid vapor selectively removes the copper oxide scale from the metallic copper. Via density functional theory, with finite temperature and pressure free energy corrections, we evaluate the feasibility of formation of gas-phase Cu(II) and Cu(I) complexes with formate, water, formic acid, and combinations thereof as ligands. These complexes result from the neutralization reaction between copper oxide (CuO and Cu_2O) and formic acid, with and without water. We identified and evaluated the formation free energies of formato, formic acid, aquahydroxo, and aquaformato complexes of Cu(II) and Cu(I). Under relevant experimental pressures, we find the water-free dimeric tetra(μ-formato)dicopper(II) "paddlewheel" complex ($Cu_2(HCOO)_4$) to be the most favorable etching product, with its formation reaching equilibrium conditions from CuO. The most likely precursor for the dimer is the diformatodi(formic acid)copper(II) monomer, which favorably dimerizes under the same water-lean condition at which the dimer persists. Stabilization of gas-phase Cu (oxide) derivatives thus can be achieved through complexation, enabling gas-phase etching of Cu. This work provides complementary experimental and theoretical studies that illuminate the nature of highly controlled etching with formic acid of nanoscopic CuO(s) layers covering Cu nanoarchitectures, which is relevant for the fabrication of next-generation integrated circuits.

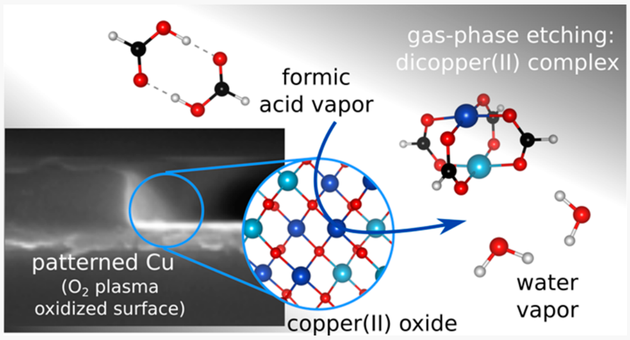

1. INTRODUCTION

Copper (Cu) has been the standard metal for interconnects in integrated circuits (ICs) since the late 1990s due to its superior conductivity and reliability, enabling smaller and faster microprocessors.[1] The perceived challenges in finding an effective, low-temperature, gas-phase etching process to pattern Cu led to the development of the Damascene and chemical-mechanical polishing (CMP) processes in which the interlayer dielectrics are patterned lithographically but do not require etching of copper.[2] While these processes eliminated the need to etch copper, other challenges arose, such as high-aspect-ratio trenches filling uniformity[3] and CMP-induced stress cracking.[4] Cu was predicted to be etchable at lower temperatures by thermodynamic analysis[5] and was achieved experimentally,[6−8] but Damascene and CMP have remained mainstream for copper integration. In recent years, 13−15 levels of metal layers are typically required to support technology nodes beyond 10 nm.[9] Figure 1 shows a high-performance, dense interconnect that meets computing needs and reliability requirements.[10] This top-heavy structure clearly constrains the fragile low-*k* material and creates a new challenge related to removing the copper overburden, which reinvigorates the need for a selective, low-temperature, gas-phase process to etch copper.[11] The most viable strategy is to develop a chemically controlled atomic layer etching (ALE) process that can pattern copper without grain-size effects and that has high selectivity toward the barrier layer.

ALE is sometimes simplistically referred to as reverse atomic layer deposition (ALD). Though that is inaccurate, intuitively, ALD studies often provide insight into what chemistries might be viable for ALE, especially in identifying potential volatile reaction products (which may be used as precursors for ALD). ALD has been instrumental in the synthesis of metals involving an oxidized metal and a reductant, "packaged" together as a gas-phase complex. At high temperatures, the metal cation is reduced by the reductant ligand, thereby depositing the metal.

Received: October 1, 2020
Revised: December 10, 2020
Published: January 12, 2021

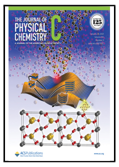

https://dx.doi.org/10.1021/acs.jpcc.0c08932
J. Phys. Chem. C 2021, 125, 1819−1832

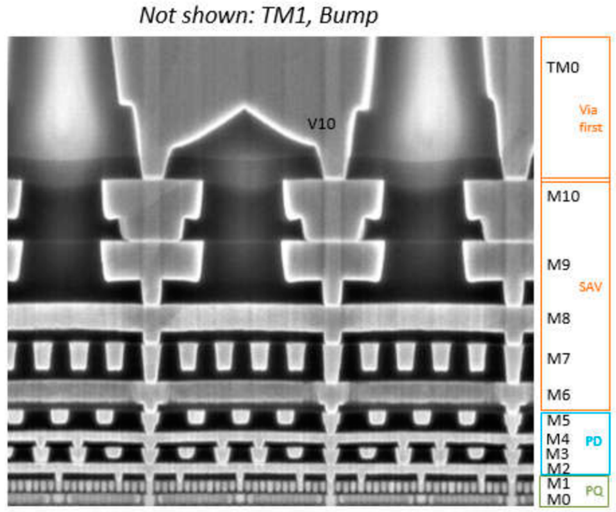

Figure 1. Illustration of the lowest 10 layers of metal (copper) of a 10 nm interconnect stack.[10] M = metal, TM = thick metal, V = via, PQ = pitched quartered, PD = pitch doubled, SAV = self-aligned via. Reprinted with permission from ref 10. Copyright 2018 IEEE.

Therefore, it is conceivable to attempt the reverse process to etch metals, where the metal surface is first oxidized, and then neutralized and complexed with a gaseous organic acid etchant. From an electrochemical standpoint, Cu(II) has a standard reduction potential to Cu(0) of 0.3419 V vs the standard hydrogen electrode (SHE), making it one of the most readily reducible metal cations to its elemental form. It is even easier for Cu(I) to reduce to Cu(0) (which also easily oxidizes to Cu(II)) due to its higher standard reduction potential of 0.521 V vs the SHE.[12] Although elemental copper is easily produced from its ionized forms via electrochemistry, such reduction reactions should only happen in closely controlled environments requiring reasonable molecular stability. More specifically, many organometallic precursors have been developed for the deposition of copper thin films at temperatures ranging from 100 to 390 °C, including bis(acetylacetonato)copper(II) and its fluorinated form bis(hexafluoroacetylacetonato)copper(II), bis(*N*,*N*′-diisopropyl-acetamidinato)copper(II), and bis(dimethylamino-2-propoxy)copper(II).[13] These results suggest that copper may be etchable by selected organic chemistries, with tailored oxidation states.

Computational methods based on density functional theory (DFT), with at least gradient-corrected exchange-correlation functionals, now routinely provide atomic-scale understanding of many ground-state chemical reactions and materials properties.[14−18] DFT-based simulations have been instrumental to innovations in the fields of photovoltaics,[19−21] (photo)-electrocatalysis,[22−27] energy storage devices,[28,29] and materials (bulk and surface) processing[30−33] to name a few. It has become an enabling approach for functional material design and chemical process development and has been used to evaluate gas-phase chemical processes relevant to the semiconductor industry, including chemical vapor deposition (CVD) and ALD of copper.[34,35] More recently, DFT has provided understanding of surface reactions during ALE of aluminum oxide and polymers.[36,37] While ALE of copper has been reported recently experimentally,[38−40] quantification of the volatile reaction products has been challenging due to their low concentrations. It is therefore the goal of this work to combine experimental studies and theoretical insight to delineate the most probable reaction mechanism leading to selective ALE of copper.

Specifically, gas-phase formic acid (HCOOH) is used here to demonstrate its capability to react preferentially with Cu oxide over Cu metal at a relatively mild temperature (80 °C). Although HCOOH has been utilized as a reducing agent for CVD and ALD of Cu,[41−45] the mechanism that leads to etching is believed to be via acid−base reaction between HCOOH and Cu oxide, resulting in the formation of gaseous neutralization products, namely, water vapor ($H_2O(g)$) and Cu(II)-formato complexes. Decomposition of HCOOH on Cu and Cu oxide, which generally only occurs at temperatures greater than 180 °C, simply reduces the oxide back to its metallic form and does not lead to etching.[46,47] Leveraging the above-mentioned etching selectivity for the oxide, we have developed a two-step cyclic process, consisting of: (1) oxidation via exposure to O_2 plasma to form a surface copper-oxide layer and (2) selective removal of the oxide layer via etching with HCOOH vapor, leaving a pristine metal Cu surface behind. This process can be repeated for continual layer-by-layer removal of Cu, where the control of etch rate and anisotropy can be demonstrated through tuning of the O_2 plasma processing conditions. Exploration via DFT calculations of various gas-phase complexes of Cu(II) with formate, formic acid, and water suggests that gaseous monomeric and dimeric aquaformato and formato Cu(II) complexes are the most likely to form, rationalizing the observed oxide etching. Although experimentally CuO is not expected to reduce to Cu_2O upon exposure to formic acid at temperatures lower than ∼200 °C,[48] we also investigated computationally the formation of Cu(I) complexes as etching products. Cu(I) etching was found to be more thermodynamically difficult and therefore would be less likely to participate in etching even if present.

2. METHODS

2.1. Experiment. Two Cu blanket thin films were utilized to assess the effectiveness of the etching processes, both prepared by sputter-deposition, one with a thickness of 70 nm and one with a thickness of 25 nm. The thicker sample was used for solution-phase etching to more easily quantify the etch rate. The thinner sample was used for ALE processing. Copper oxide thin films were obtained by heating the thicker Cu stack at 150 °C for 1 h in air, which led to an observed volumetric expansion of around 60%, in line with the Pilling−Bedworth ratio for Cu. This annealing process leads to the formation of mainly CuO with some $Cu(OH)_2$ (CuO_x is used to collectively denote the oxide formed). Additionally, one patterned Cu sample was used to evaluate the etching anisotropy and profile control: a 55 nm Cu sample, with a Ta barrier layer with a 135 nm thick SiCN hard mask that is patterned into 6.5 and 1.5 μm lines with 4.5 and 2 μm spacings. The atomic composition and chemical states of Cu were obtained using X-ray photoelectron spectroscopy (XPS, Kratos XPS Axis Ultra DLD, with 40 eV passing energy). To quantify the etch rate, the thickness of Cu was imaged by cross-sectional scanning electron microscopy (SEM, FEI Nova 600, with 10 keV electron beam energy), before and after the etching process. The line scan route is labeled on top-down SEM images to compare the spatial distribution of elements of interest between samples before and after treatments. The elemental distribution on patterned samples were examined by energy dispersive spectroscopy (EDS, FEI NOVA 230, with 10 keV electron beam energy).

For solution-phase etching, stock solutions of HCOOH (95%, Sigma-Aldrich) were maintained at a constant temperature of 80 °C utilizing a water bath. Cu and CuO_x samples were submerged in the stock solutions for a specified period of time, rinsed in deionized H_2O and dried by nitrogen (ultrahigh purity (UHP), Airgas).

For gas-phase etching, a cyclic oxidation−formic acid exposure process was developed. For the oxidation half-cycle, an oxygen (UHP, Airgas) plasma was generated at 30 mTorr in an etcher (Unaxis 770) with a radio frequency (rf) source power of 500 W. The samples were placed on a carrier wafer which received an applied bias ranging from 0 to 50 W, with no additional heating, for 1−2 min. For the formic acid half-cycle, a custom-built, hot-walled, vacuum reactor homemade with a base pressure of 0.8 Torr was used. To introduce HCOOH into the chamber, high-purity nitrogen (UHP, Airgas, 100 sccm) and HCOOH (95%, Sigma-Aldrich, in a glass ampule) at a flow rate of 0.1 g/min were introduced into a temperature-controlled vaporizer (HORIBA MI-1000) at 80 °C. In the chamber, the total pressure was kept at 250 Torr. The total chamber pressure is attributed primarily to the etchant mixture ($HCOOH+N_2$) and therefore used as a basis for determination of the pressure of the etchant during the formic acid half-cycle. For DFT simulations (vide infra) two pressures were studied, namely, 250 and 125 Torr as upper and lower bounds of the vapor pressure of HCOOH, respectively. The samples were placed in the chamber where the chamber wall was held at 80 °C for all experiments. These two process steps (oxidation and formic acid exposure) can be repeated as a cycle, with a 5 min vacuum break between oxidation and formic acid vapor exposure.

2.2. Theory and Simulation.

All of the simulations were performed within the projector augmented-wave (PAW)[49] periodic-planewave DFT formalism as implemented in the Vienna Ab-initio Simulation Package (VASP) version 5.4.4.[50] The Perdew−Burke−Ernzerhof (PBE) exchange-correlation functional was used in the evaluation of the Kohn−Sham electronic energies.[51] PAW potentials were used for all elements, with frozen core orbitals of 1s for C and O, and (1s2s2p3s3p) for Cu. The simplified rotationally invariant effective Hubbard U correction[52] (+U) was included for Cu 3d orbitals (U = 3.6 eV, derived from unrestricted Hartree−Fock theory on electrostatically embedded Cu_2O clusters[53]). van der Waals interactions were simulated via the D3 method with Becke−Johnson damping (D3BJ).[54,55] A 660 eV planewave basis kinetic-energy cutoff was imposed. A Gaussian electronic smearing (0.01 eV) was applied. The electron spin of Cu(II) was initialized with one unpaired electron, as expected for a valence d^9 transition metal. The Cu(II) ion(s) in all species, bulk and molecular complexes, converged to an absolute projected net electronic spin of approximately 0.6−0.7 e, thus confirming the existence of Cu(II). Cu(I)-containing species were simulated spin-unpolarized, since Cu(I) has a closed-shell d^{10} electronic valence.

2.2.1. Solid-Phase Oxides. An absolute atomic force threshold of 0.002 eV/Å was imposed during lattice vector and atomic-position optimizations. To reduce numerical noise in forces and stresses, the fine-grid fast Fourier transform (FFT) was set to 4 times the coarse FFT, and the PAW core compensation charge was evaluated at 8 times the default grid. The converged lattice vectors of the various antiferromagnetic (AFM) and ferromagnetic (FM) monoclinic CuO (Figure S1), orthorhombic $Cu(OH)_2$ (Figure S2), and their respective Brillouin zone (k-point) sampling, are summarized in Tables S1 and S2. The pristine cubic Cu_2O has no unpaired electrons; therefore, no optimization of the magnetic structure was performed. The Cu(I) oxide's optimized lattice parameters and accompanying k-point sampling are in Table S3. The phonon frequencies of the three solids were calculated by generating multiple finite atomic displacements (±0.01 Å from equilibrium) using phonopy (version 2.4.1)[56] and calculating atomic forces using VASP. The subsequent postprocessing to obtain the phonon densities of states (phDOS) and vibrational free energy contributions (Table S4) were performed also using phonopy. The solids' phDOS (Figure S3) confirm the stability of the optimized crystal structures found.

2.2.2. Gas-phase molecules. A periodic box size of 22 × 22 × 18 $Å^3$ was used to isolate the gas-phase HCOOH, $(HCOOH)_2$, H_2O, CO_2 molecules and Cu(II) and Cu(I) complexes (vide infra), with a dipole correction applied in all directions, which include corrections for both the energy and potential.[57,58] A Γ-point-only k-point sampling was employed. An absolute atomic force threshold of 0.01 eV/Å was imposed for atomic structure optimization. The vibrational frequencies were evaluated within the harmonic approximation, with the Hessians constructed via the finite atomic displacement method (±0.02 Å from equilibrium). The calculation of the free energy contributions from the translational, rotational, and vibrational degrees of freedom are described in the Supporting Information, methods section I (Tables S4 and S5). Benchmarking of the same DFT parameters used here for both gaseous HCOOH and $(HCOOH)_2$ are available in ref 59.

The free energy of the gaseous O_2 molecule at temperature $T(G(O_2(g), T))$ was calculated from the DFT energy of an O atom (E_O^{DFT}, spin = 2 μ_B, simulated in a 22 × 20 × 18 $Å^3$ box), its translational free energy at $T(G_{trans}(O(g), T)$, Supporting Information, methods section I; Tables S4 and S5), and the experimental formation free energy of gaseous O atom at $T(\Delta G_f^{exp}(O(g), T)$, taken from the NIST-JANAF database:[60]

$$G(O_2(g), T) = 2(E_O^{DFT} + G_{trans}(O(g), T) - \Delta G_f^{exp}(O(g), T))$$

The O_2 molecule was not explicitly modeled in DFT because PBE is known to overstabilize the molecule; it overestimates the molecule's atomization energy by as much as 1 eV/O_2.[51]

3. RESULTS AND DISCUSSION

3.1. Etching Copper in Organic Solutions.

To determine the etch selectivity of Cu compared to CuO_x via reaction with formic acid, solution-phase etching was first performed. Figure 2 shows a plot of film thickness as a function of time for Cu and CuO (CuO_x sample thickness is 110 nm due to expansion from thermal oxidation); it is evident that the etch rate is significantly higher for the oxide as compared to the metal. Figure 2 shows the evolution of residual CuO_x as a function of etch time. Due to the inhomogeneity of the solution phase etch (Figure S4) at very short times, an accurate etch rate was difficult to determine from the slope of the curve. However, a conservative etch rate can be estimated at the longest etch time (10 s) to be ~520 nm/min. In comparison to the etch rate of Cu (1.7 nm/min), the selectivity would be >300 (calculated from the ratio of the etch rates). Although the selectivity is large for etching CuO over Cu in HCOOH solution, the use of a solution process is not desired due to the isotropic nature of the etching process that can undercut the

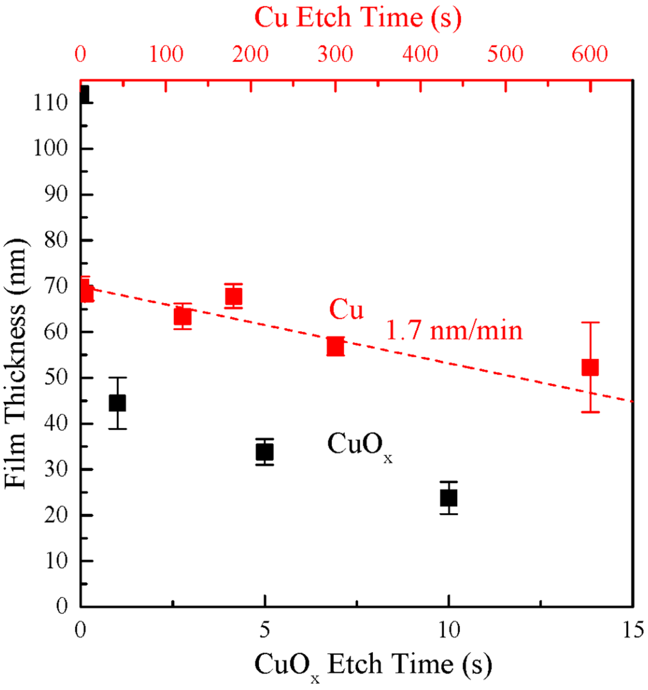

Figure 2. Remaining film thickness as a function of etching time for copper and copper oxide in formic acid solution at 80 °C. The Cu sample consisted of a 70 nm Cu layer deposited on a 15 nm TiN layer on Si. Thermal oxidation of the 70 nm Cu layer was performed via annealing under ambient conditions, where the film had expanded to ~110 nm post thermal oxidation. The selectivity for etching CuO over Cu in HCOOH solution is >300. Note the difference in red versus black time scales.

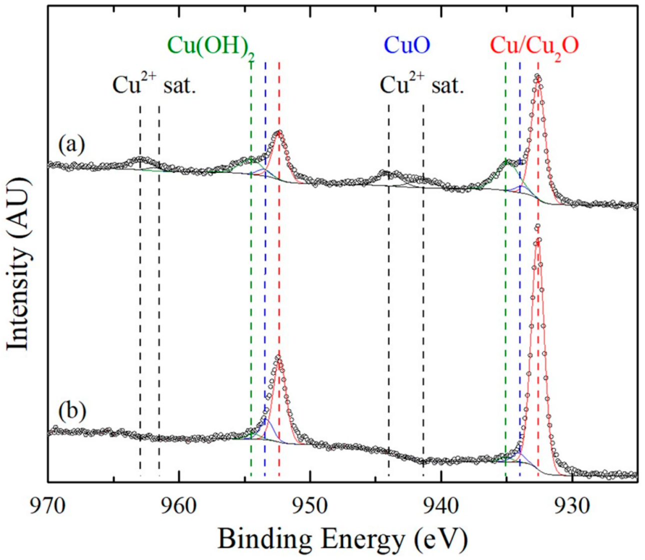

Figure 3. XPS Cu 2p spectra from a 25 nm Cu film in the (a) as-deposited state and (b) post-HCOOH-vapor-exposure (20 min, 250 Torr (HCOOH, under N_2), 80 °C). The copper feature was deconvoluted into Cu(0), Cu(I), Cu(II), and $Cu(OH)_2$ states, along with satellite (sat.) peaks. The copper native oxide layer was removed by the formic acid vapor but metallic copper remained.

features under a mask. It is also difficult to completely remove the remaining chemical, due to the surface tension effect, from the nanoscale-patterned surface features.

3.2. Etching Copper by Gas Phase Organics. Having established the selectivity of etching copper oxide versus copper metal to be >300 in the HCOOH solution, the corresponding selectivity in HCOOH vapor was determined. Figure 3 shows high-resolution XPS spectra over the Cu 2p region for the (a) as-deposited Cu as well as (b) a sample treated with 250 Torr HCOOH (with N_2 as carrier gas) for 20 min at 80 °C. XPS was performed ex situ, but air exposure was minimized between HCOOH exposure and characterization. As can be seen in the XPS spectra, the reduction of Cu $2p_{3/2}$ peaks associated with $Cu(OH)_2$(934.5 eV) and CuO (933.5 eV)[61] as well as Cu(II) $2p_{3/2}$ satellite (sat.) features at 944.5 eV was consistent with the removal of Cu(II) oxide. Cu_2O and Cu could not be resolved at the resolution of the spectrometer (difference ~0.1 eV), where Cu_2O has been observed to form first upon native oxide formation.[62] To better distinguish different Cu species, the Cu LMM Auger line also was examined; the transition from Cu^0 to Cu^{2+} post oxidation was clearly observed (Figure S5). Imaging by SEM of both samples (not shown) confirmed that only the native oxide was removed and that no measurable etching of the metallic copper was observed.

To leverage the etch selectivity of Cu via CuO_x with HCOOH vapor, an ALE approach was taken, consisting of plasma oxidation followed by self-limiting removal of the oxide layer by HCOOH vapor. Therefore, controlled etch and subsequent Cu removal can be finely controlled by the oxidation step in which O_2 plasma as an oxidant modulates the etch anisotropy though substrate biasing. The process approaches self-limiting behavior for both half-steps when the oxidation conditions produce a diffusion-limited oxide layer. A cyclic etch process consisting of an O_2 plasma oxidation step (500 W rf power, 0 W bias, 2 min) and a formic acid vapor step (250 Torr HCOOH (with N_2) at 80 °C, 5 min) was performed for several cycles on a 25 nm Cu film. An etch rate of 2.4 nm/cycle was observed at the conditions tested (Figure 4a). Figure 4b shows the high-resolution XPS spectra of the Cu 2p region for the as-deposited film and after 4 and 8 cycles of ALE, where the Cu was nearly completely removed.

3.3. Etching of Patterned Copper Thin Film. The process described above was then applied to patterned Cu samples to assess profile control. The patterned sample was first treated with a 2 min oxidation for cleaning mask opening residue at 800 W rf and 70 W applied bias. During this pretreatment process, around 55 nm of the hard mask was removed, but the Cu layer was not etched. Figure 4 shows the comparison between the as-patterned Cu thin film before and after 5 cycles consisting of an oxidation step (500 W rf power and 0 W applied bias for 2 min) and a HCOOH (with N_2) exposure (250 Torr, 80 °C for 5 min). The cross-sectional SEM images (Figure 5a,b) show that Cu in the exposed region was completely removed, with limited change in the hard mask thickness during the cyclic process utilizing oxygen plasma at lower power and bias. Top-down SEM images (Figure 5c,d) were taken of regions in close proximity before and after the process to compare the profile; the brighter regions in the pretreatment sample image correspond to the exposed Cu while the darker regions are those blocked by the SiCN hard mask. EDS line scans (Figure 5e,f), along highlighted arrows in Figure 5c,d, chemically confirmed the removal of Cu from the sample surface. The Cu signal intensity, denoted by the black curve, decreased drastically from the masked to the exposed region on the treated sample, as compared to the uniform intensity observed for the as-deposited sample. Partial removal

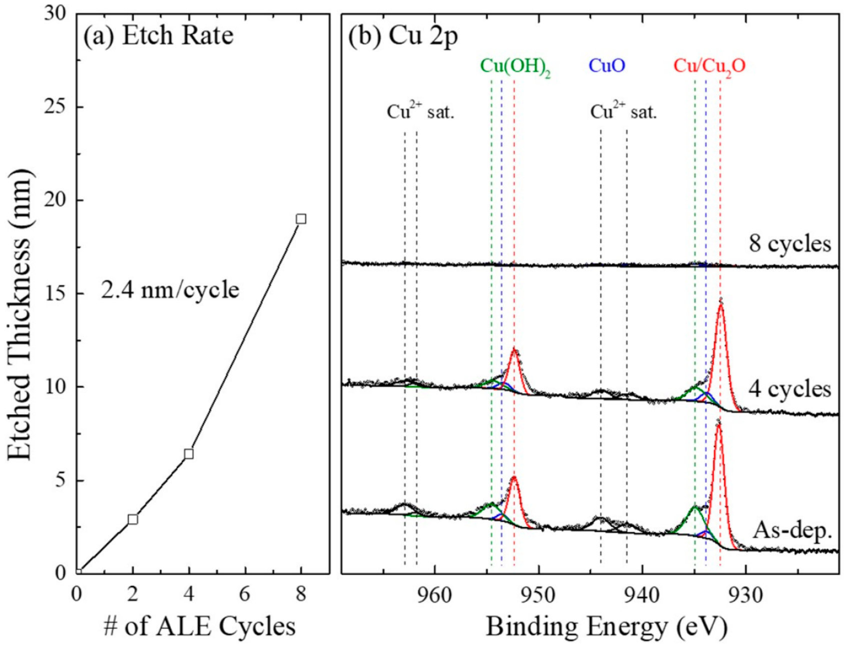

Figure 4. (a) Thickness change of 25 nm Cu by cycles of O_2 plasma and formic acid vapor, as determined via cross-section SEM with 2 min oxidation (500 W, 0 W bias, 35 mTorr) and 5 min HCOOH vapor exposure (250 Torr (formic acid with N_2), 80 °C). (b) Corresponding high-resolution XPS spectra of the Cu 2p spectra, confirming the removal of copper.

of the SiCN hard mask was noted from the SEM images before and after etching, which is not a concern for verifying the validity of the etching chemistry since the line width remains constant and the underlying Cu was protected from oxidation and etching.

3.4. DFT Simulations. The relatively large volume of the chamber compared to the miniscule amounts of etched material made direct characterization of the etching products difficult. HCOOH vapor clearly directly interacts with the oxide layer, CuO, and $Cu(OH)_2$; however, the reaction product and its fate in the chamber is unknown. As in the solution-phase etching, the CuO (and $Cu(OH)_2$) is expected to react with HCOOH via an acid−base (neutralization) reaction, followed by complexation with either water and hydroxide, unreacted HCOOH and its conjugate base formate ($HCOO^-$), or some combination. Thermodynamics indicate that HCOOH also may act as a reducing agent, enabling the formation of Cu_2O from CuO. The Cu LMM Auger line XPS spectra in Figure S5 show no Cu_2O after plasma O_2 oxidation, but it suggests its emergence after etching (it is also possible that the vacuum break prior to the XPS measurement post etching may have introduced the Cu(I) species along with the hydration of residual CuO to $Cu(OH)_2$). Below, we present first the complexation and etching of Cu(II) from CuO and $Cu(OH)_2$. This is followed by an exploration of the possible participation of Cu(I) species, from Cu_2O, in the formation of volatile Cu species. Lastly, we assess the thermodynamics of the formation of gaseous neutral Cu(II) and Cu(I) molecular complexes under likely experimental conditions.

3.4.1. Etching through Neutralization and Complexation of Cu(II)OH$_x$. To explore the gas-phase complexes of Cu(II) with water/hydroxide, formic acid, and $HCOO^-$, various Cu(II) complexes were investigated by means of DFT approximations. Figure 6 summarizes the optimized structures of the various complexes that may form, which include both Cu(II) monomer and dimer complexes. Note that only neutral complexes were studied, because unlike in aqueous phase generation of gaseous charged species off of the CuO/$Cu(OH)_2$ surface is not stabilized by a polarizable medium, e.g., bulk water, and therefore will be extremely unfavorable. Starting from the monoclinic AFM CuO, Figure 6 shows in sequence the formation of complexes, growing from two coordinating ligands to five (blue paths, **a**−**d**), and from monomer to dimer (violet paths, **f**−**h**). Also in the figure is the reaction connecting CuO and $Cu(OH)_2$ (orange path, **j**). The AFM structures of CuO and $Cu(OH)_2$ are shown through two different blue-colored Cu ions, one for excess electron spin-up and another for excess electron spin-down. For CuO, FM interactions persist along the [010] and [101] directions, with alternating AFM and FM interactions along the [$10\bar{1}$], as demonstrated in the literature.[63,64] For $Cu(OH)_2$, FM interactions exist along [001] and [100], with alternating AFM and FM interactions along [010].

Although the complexation reactions are presented in sequence in Figure 6, they need not proceed in this manner. In this study, only the thermodynamics was assessed for the formation of these complexes, with CuO/$Cu(OH)_2$, water vapor, and formic acid as reactants (as a dimer $(HCOOH)_2$, which is the majority form of HCOOH in the gas phase,[65] Figure S6). Although kinetics may play a role in the feasibility of forming these chemical species, thermodynamics of course is needed to set the stage in determining possible chemical pathways. Table 1 lists the standard reaction free energies at three different temperatures, namely, room, experimental (T = 353 K (80 °C)), and "extreme" (T = 403 K; 29° above the boiling point of HCOOH), along with the chemical equations representing the reactions in Figure 6. Three temperatures were given to illuminate the dependence of the spontaneity of these reactions with temperature. From these standard reaction free energies, the nonstandard reaction free energies under a (likely) range of experimental reactant and product partial pressures (vide infra) can be extrapolated.

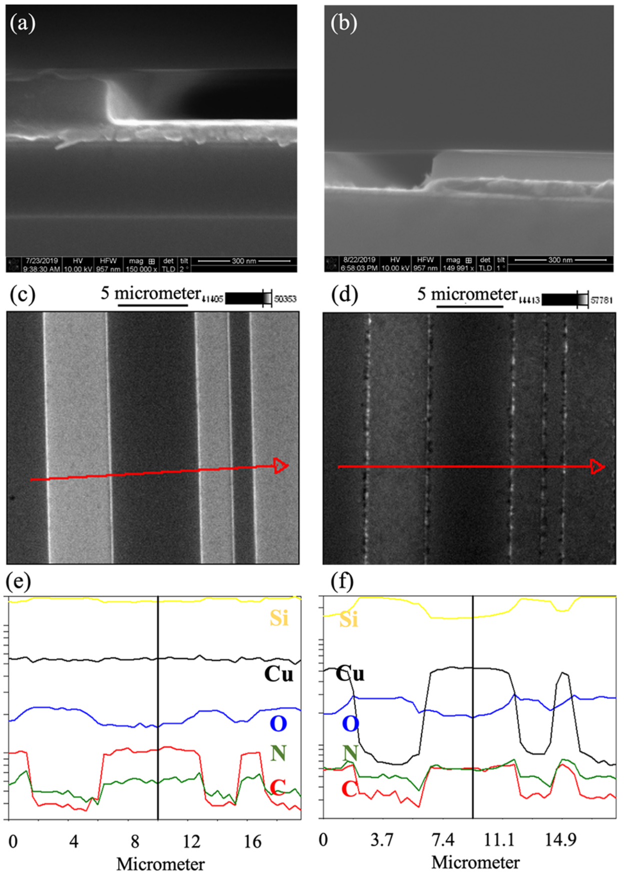

Figure 5. Characterization of the cyclic etch process (described in the main text) on patterned Cu. SEM cross-sectional image of (a) as-deposited patterned Cu and (b) processed patterned Cu. Top-down SEM of (c) as-deposited patterned Cu and (d) processed patterned Cu, with EDS line scan routes indicated by the arrows. EDS line scans along the arrows of the (e) as-deposited patterned Cu and (f) processed patterned Cu.

Reaction **a** in Figure 6 describes the formation of the diformatocopper(II) complex ($Cu(\kappa^2\text{-}HCOO)_2$) from $(HCOOH)_2$ reacting with a unit of CuO, releasing water. $HCOO^-$ is a bidentate ligand, κ^2, which means it has two noncontiguous coordinating atoms: the two O atoms. The two protons from $(HCOOH)_2$ form a water molecule with an O in the CuO lattice (acid−base or neutralization reaction), while the resulting two $HCOO^-$ ions coordinate with a Cu(II) ion (complexation). This reaction is highly unfavorable with a standard free energy of reaction of $\Delta G^\circ \sim 1$ eV (Table 1). $Cu(\kappa^2\text{-}HCOO)_2$ exhibits a square planar structure, as in the bulk CuO (Figure 6). However, the molecule may be in a nonideal, constrained configuration. Cu(II) is a d^9 transition metal cation (one unpaired electron) that forms tetrahedral, square planar, or some intermediate coordination, the preference of which depends on the ligand and even the counterion.[67]

Cu(II) can only accommodate two formate ions to maintain a neutral complex, thus to build larger neutral mononuclear complexes, only a neutral ligand, such as H_2O, can be added. Reactions **b** and **c** progressively relieve the strain in the complex by adding H_2O as ligand, converting an $HCOO^-$ from being a bidentate (κ^2) to a monodentate (κ^1) ligand for every H_2O added: $Cu(H_2O)(\kappa^1\text{-}HCOO)(\kappa^2\text{-}HCOO)$ or simply $Cu(H_2O)(HCOO)_2$, and $Cu(H_2O)_2(\kappa^1\text{-}HCOO)_2$ or simply $Cu(H_2O)_2(HCOO)_2$. Furthermore, the uncoordinated O atom of the $\kappa^1\text{-}HCOO^-$ ligand forms a hydrogen bond with the coordinated H_2O. The addition of two H_2O molecules is favorable under standard conditions (Table 1), despite it being entropically unfavorable (note that the reaction becomes less spontaneous as the temperature increases). This attests to the structural (and perhaps to some degree electrostatic) nature of the significant stabilizing effect of H_2O. Indeed, in reaction **d**, where a third H_2O is added simply as an axial ligand, the process becomes unfavorable. This is because the third H_2O, in contrast to the first two H_2O, does not reduce the strain in the coordination of the equatorial ligands and because Cu(II) favorably accommodates only up to four ligands (the antibonding d_{z^2}-derived orbital of a square-planar-coordinated Cu(II) is fully occupied).

Higher-energy alternative structures for $Cu(HCOO)_2$, $Cu(H_2O)(HCOO)_2$, and $Cu(H_2O)_2(HCOO)_2$ complexes are shown in Figure S7. In the alternative $Cu(HCOO)_2$, the two $HCOO^-$ ions are bound via a κ^1 motif, leaving Cu(II) with only two bonds. The higher-energy $Cu(H_2O)(HCOO)_2$ and $Cu(H_2O)_2(HCOO)_2$ in Figure S7, however, maintain the κ^2 bonding motif for $HCOO^-$ ions, with H_2O as axial ligand(s) of Cu(II). These structures thus retain the strained square planar geometry exhibited by $Cu(\kappa^2\text{-}HCOO)_2$, while also expanding the coordination number of Cu(II) beyond four, which is unfavorable.

In the absence of water, formic acid can take the place of water as a neutral ligand, with the carbonyl oxygen as the coordinating atom. Reaction **e** (first blue-green path) shows the formation of *trans*-$Cu(\kappa^1\text{-}HCOO)_2(HCOOH)_2$ in an *eclipsed* configuration, or simply $Cu(HCOO)_2(HCOOH)_2$, from $Cu(HCOO)_2$. The trans prefix refers to the relative position of the two HCOOH, where they are opposite to each other, where the same is true for the two $HCOO^-$. In the complex, $HCOO^-$ is hydrogen bonded to a neighbor HCOOH. Since the HCOOH−OOCH hydrogen-bonded pairs are on the same side of the (distorted) CuO_4 plane, we refer to this configuration as *eclipsed*. Two of its higher-energy isomers, the *trans-staggered* conformer (the HCOOH−OOCH hydrogen-bonded pairs are on the opposite sides of the CuO_4 plane) and a *cis* isomer, are presented in Figure S7. Under standard conditions, the addition of two neutral HCOOH onto $Cu(HCOO)_2$, much like the addition of two water molecules, is favorable (Table 1, reaction **e**). The standard free energy of this addition reaction is −0.33 eV at 298 K, just 0.14 eV less negative than that of the addition of two waters, which is −0.47 eV at 298 K (Table 1, **b** + **c**).

The possibility of forming gaseous aquahydroxo complexes from $Cu(OH)_2$ (Figure S8) was examined, to rule out the need for $HCOO^-$ to directly participate in the complexation of Cu(II). Indeed, the formation of the aquahydroxo complexes is much more difficult, with standard free energies of formation relative to $Cu(OH)_2$ and $H_2O(g)$ > 1.6 eV/complex at 298 K, which highlights the critical role of $HCOO^-$ in the removal of Cu(II). This finding is consistent with the very low solubility of $Cu(OH)_2$ in pure water ($K_{sp} = 2.2 \times 10^{-20}$).[67]

Dimerization of the complex can satisfy the coordination sphere of Cu(II), while using less molecules as ligands and also relieving bonding strain. This would enable the reduction of the entropic penalty of producing the complex by using less gaseous reactants per Cu(II) ion etched. The bidenticity of the $HCOO^-$ ion make dimerization possible by acting as a bridging ligand (μ). The purple paths (**f**−**h**) in Figure 6

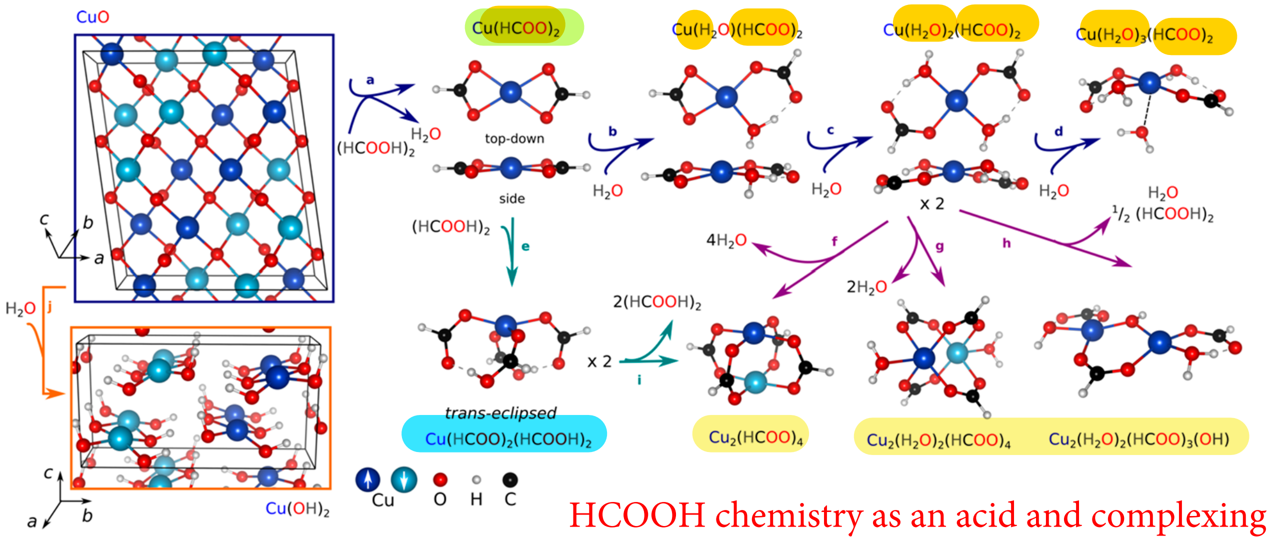

HCOOH chemistry as an acid and complexing agent

Figure 6. DFT-predicted candidate gas-phase products from etching crystalline CuO and $Cu(OH)_2$ in the presence of formic acid and water vapor. Reactions are indexed from **a** to **I**. The product molecules are formato (product of reaction **a**) and aquaformato (**b**−**d**), and diformatodi(formic acid) (**e**) complexes of Cu(II). Dinuclear formato (**f**) and aquaformato (**g** and **h**) complexes are products of the dimerization of $Cu(H_2O)_2(HCOO)_2$ releasing water (**f** and **g**) or both water and formic acid (**h**). An alternative path for dimerization is through the diformatodi(formic acid) complex (**i**). Hydration of CuO to $Cu(OH)_2$ (**j**). Two different colors of Cu denote distinct electron spins and illustrate the AFM ordering in both CuO and $Cu(OH)_2$. The dimeric Cu complexes $Cu_2(HCOO)_4$ and $Cu_2(H_2O)_2(HCOO)_4$ prefer AFM interactions, while $Cu_2(H_2O)_2(HCOO)_3(OH)$ prefers a FM ordering (Table S6).

describe formation of the candidate dimers from the most stable (under standard pressure and temperature) monomer: $Cu(H_2O)_2(\kappa^1\text{-}HCOO)_2$. Reaction **f** is the formation of the paddlewheel complex $Cu_2(\mu\text{-}HCOO)_4$ or tetra(μ-formato)-dicopper(II), which sheds all four H_2O molecules from the two $Cu(H_2O)_2(\kappa^1\text{-}HCOO)_2$ molecules. The four $HCOO^-$ bridge the two Cu(II) ions with the two $Cu(O)_4$ planes on top of each other, forming a paddlewheel-like structure (Figure 6), hence the name. Reaction **g** is a similar reaction, but expels one less H_2O molecule per Cu(II), forming a fully hydrated paddlewheel complex: $Cu_2(H_2O)_2(\mu\text{-}HCOO)_4$, with two H_2O as axial ligands (Figure 6). The formations of these complexes are mildly favorable (−0.11 and −0.10 eV/Cu) relative to $Cu(H_2O)_2(\kappa^1\text{-}HCOO)_2$ at 353 K, which become more favorable at higher temperatures, e.g., −0.21 and −0.14 eV/Cu at 403 K, because these reactions result in a net positive formation of gaseous molecules (Table 1, reactions **f** and **g**). An alternative monomer that may serve as a precursor to $Cu_2(\mu\text{-}HCOO)_4$ in the absence of water is $Cu(HCOO)_2(HCOOH)_2$. Dimerization is achieved by shedding two $(HCOOH)_2$ molecules per $Cu_2(\mu\text{-}HCOO)_4$ (Figure 6, reaction **i**, second blue-green path). Similar to the aqua analogue, this dimerization reaction is exoergic (−0.15 eV/Cu at 353 K). Paddlewheel transition-metal complexes are well-documented in the literature,[68] with Cu(II)-based complexes containing large organic carboxylates achieving prominence because of its central chemical motif in many metal organic frameworks (MOFs).[69,70] Earlier documentation of Cu(II) paddlewheel complexes involved small organic carboxylates, such as crystalline hydrated tetraacetatodicopper(II), $Cu_2(H_2O)_2(\mu\text{-}CH_3COO)_4$,[71] and anhydrous tetrapropionato-dicopper(II), $Cu_2(\mu\text{-}C_2H_5COO)_4$, dissolved in chloroform.[72] Recently, infrared multiphoton dissociation has been shown to decompose anionic copper(II) formate clusters of the formula $Cu(II)_n(HCOO)_{2n+1}^-$ ($2 < n \leq 8$, generated via electrospray ionization or ESI), proceeding via favorable sequential loss (evaporation) of neutral dimeric $Cu_2(HCOO)_4$ until $n = 3$, at which point $Cu(HCOO)_2$ is released.[73] The aforementioned observation was supported by the authors' DFT-B3LYP/def2TZVP simulations.[73]

For reaction **h**, $Cu_2(H_2O)_2(HCOO)_3(OH)$ or $Cu_2(H_2O)_2(\mu\text{-}HCOO)(\kappa_1\text{-}HCOO)_2(\mu\text{-}OH)$ forms where both an $HCOO^-$ and an OH^- act as bridging ligands. It consists of two complexes side-by-side, instead of being on top of each other as in the paddlewheel complexes. This reaction has similar thermodynamics as **f** and **g** but exhibits weaker dependence on temperature than **f** and **g**, because it results in fewer gaseous products compared to the other two reactions.

3.4.2. Etching after Pre-Reduction of Cu(II)O into $Cu(I)_2O$.

So far, we viewed HCOOH chemistry as an acid and complexing agent. In this section we explore the possibility of HCOOH acting also as a reductant. Reduction of CuO to Cu_2O with HCOOH as a reducing agent is thermodynamically feasible. In this reaction, HCOOH oxidizes into CO_2, while two Cu(II) ions reduce to Cu(I) as the two H atoms from the decomposition of HCOOH remove an O atom from the lattice to form H_2O. The empirical standard reaction free energy at 298 K for this rection is −0.81 eV/CuO, while we predict it to be −0.71 eV/CuO, an approximately 0.1 eV error (Table 1). At the experimental etching temperature (353 K) and $(HCOOH)_2$ pressure (approximately within 125−250 Torr, see below for the rationale of the estimates), the reaction is predicted to remain spontaneous (Figure 7a, blue lines). We set the CO_2 and H_2O partial pressures at 0.08 Torr or 1/10 of the vacuum base pressure (0.8 Torr, this pressure was imposed prior to the introduction of HCOOH+N_2 mixture into the reaction chamber, section 2.2). In Figure 7a, the experimental and theoretical data at 298 K are also plotted to provide an estimate to the error of the prediction at 353 K. A competing reaction that will oxidize Cu_2O back to CuO is via reaction with molecular oxygen. The standard oxidation free energy at 298 K has been also measured to be very negative: −0.56 eV/CuO. PBE+*U*+D3BJ overestimates the exoergicity of this

Table 1. Standard Reaction Free Energies (eV/Cu at Standard 750 Torr Pressure) for the Formation of Cu(II) and Cu(I) Formato, Formic Acid, and Aquaformato Complexes and Bulk Phase Reactions Involving $Cu(OH)_2$, CuO, and Cu_2O as Depicted in Figures 6 and 7[a]

reaction index	reaction equation	298 K	353 K	403 K
a	$CuO + (HCOOH)_2 \rightarrow Cu(HCOO)_2 + H_2O$	0.95	**0.85**	0.77
b	$Cu(HCOO)_2 + H_2O \rightarrow Cu(H_2O)(HCOO)_2$	−0.27	**−0.19**	−0.12
c	$Cu(H_2O)(HCOO)_2 + H_2O \rightarrow Cu(H_2O)_2(HCOO)_2$	−0.20	**−0.11**	−0.03
d	$Cu(H_2O)_2(HCOO)_2 + H_2O \rightarrow Cu(H_2O)_3(HCOO)_2$	0.13	**0.19**	0.25
e	$Cu(HCOO)_2 + (HCOOH)_2 \rightarrow Cu(HCOOH)_2(HCOO)_2$	−0.33	**−0.26**	−0.20
f	$Cu(H_2O)_2(HCOO)_2 \rightarrow \frac{1}{2}Cu_2(HCOO)_4 + 2H_2O$	0.00	**−0.11**	−0.21
g	$Cu(H_2O)_2(HCOO)_2 \rightarrow \frac{1}{2}Cu_2(H_2O)_2(HCOO)_4 + H_2O$	−0.06	**−0.10**	−0.14
h	$Cu(H_2O)_2(HCOO)_2 \rightarrow \frac{1}{2}Cu_2(H_2O)_2(HCOO)_3(OH) + \frac{1}{2}H_2O + \frac{1}{4}(HCOOH)_2$	−0.04	**−0.06**	−0.08
i	$Cu(HCOOH)_2(HCOO)_2 \rightarrow \frac{1}{2}Cu_2(HCOO)_4 + (HCOOH)_2$	−0.14	**−0.15**	−0.16
j	$CuO + H_2O \rightarrow Cu(OH)_2$	0.08[b]	**0.17**	0.25
M1 = **a** + **b** + **c**	$CuO + (HCOOH)_2 + H_2O \rightarrow Cu(H_2O)_2(HCOO)_2$	0.48	**0.55**	0.62
M2 = **a** + **e**	$CuO + 2(HCOOH)_2 \rightarrow Cu(HCOOH)_2(HCOO)_2 + H_2O$	0.62	**0.60**	0.57
D1 = M1 + **f**	$CuO + (HCOOH)_2 \rightarrow \frac{1}{2}Cu_2(HCOO)_4 + H_2O$	0.48	**0.44**	0.41
D2 = M1 + **g**	$CuO + (HCOOH)_2 \rightarrow \frac{1}{2}Cu_2(H_2O)_2(HCOO)_4$	0.41	**0.45**	0.48
D3 = M1 + **h**	$CuO + \frac{3}{4}(HCOOH)_2 + \frac{1}{2}H_2O \rightarrow \frac{1}{2}Cu_2(H_2O)_2(HCOO)_3(OH)$	0.44	**0.49**	0.54
	$CuO + \frac{1}{4}(HCOOH)_2 \rightarrow \frac{1}{2}Cu_2O + \frac{1}{2}CO_2 + \frac{1}{2}H_2O$	−0.71[c]	**−0.75**	−0.78
	$\frac{1}{2}Cu_2O + \frac{1}{4}O_2 \rightarrow CuO$	−0.75[c]	**−0.75**[d]	−0.76[d]
a′	$\frac{1}{2}Cu_2O + \frac{1}{2}(HCOOH)_2 + \frac{1}{2}H_2O \rightarrow Cu(H_2O)(HCOO)$	1.34	**1.32**	1.29
b′	$Cu(H_2O)(HCOO) + H_2O \rightarrow Cu(H_2O)_2(HCOO)$	−0.50	**−0.41**	−0.33
c′	$\frac{1}{2}Cu_2O + (HCOOH)_2 \rightarrow Cu(HCOO)(HCOOH) + \frac{1}{2}H_2O$	0.84	**0.79**	0.75
d′	$Cu(H_2O)(HCOO) \rightarrow \frac{1}{2}Cu_2(HCOO)_2 + H_2O$	−0.84	**−0.85**	−0.86
e′	$\frac{1}{2}Cu_2(HCOO)_2 + H_2O \rightarrow \frac{1}{2}Cu_2(H_2O)_2(HCOO)_2$	0.10	**0.16**	0.22
f′	$Cu(HCOO)(HCOOH) \rightarrow \frac{1}{2}Cu_2(HCOO)_2 + \frac{1}{2}(HCOOH)_2$	−0.33	**−0.33**	−0.33
g′	$\frac{1}{2}Cu_2(HCOO)_2 + \frac{1}{2}(HCOOH)_2 \rightarrow \frac{1}{2}Cu_2(HCOO)_2(HCOOH)_2$	0.03	**0.06**	0.09
M1′ = **a′** + **b′**	$\frac{1}{2}Cu_2O + \frac{1}{2}(HCOOH)_2 + \frac{3}{2}H_2O \rightarrow Cu(H_2O)_2(HCOO)$	0.84	**0.90**	0.96
M2′ = **c′**	$\frac{1}{2}Cu_2O + (HCOOH)_2 \rightarrow Cu(HCOO)(HCOOH) + \frac{1}{2}H_2O$	0.84	**0.79**	0.75
D1′ = **a′** + **d′**	$\frac{1}{2}Cu_2O + \frac{1}{2}(HCOOH)_2 \rightarrow \frac{1}{2}Cu_2(HCOO)_2 + \frac{1}{2}H_2O$	0.51	**0.46**	0.43
D2′ = D1′ + **e′**	$\frac{1}{2}Cu_2O + \frac{1}{2}(HCOOH)_2 + \frac{1}{2}H_2O \rightarrow \frac{1}{2}Cu_2(H_2O)_2(HCOO)_2$	0.61	**0.63**	0.65
D3′ = D1′ + **g′**	$\frac{1}{2}Cu_2O + (HCOOH)_2 \rightarrow \frac{1}{2}Cu_2(HCOO)_2(HCOOH)_2 + \frac{1}{2}H_2O$	0.54	**0.53**	0.52

Table 1. continued

[a]Reactions **a**−**h** and **a′**−**g′** are combined to determine the reaction free energies in forming the most stable complexes with CuO, $(HCOOH)_2$, and H_2O as reactants. The relevant energies at experimental temperature of 353 K (80 °C) are bolded. [b]Experimental value is −0.16 eV calculated using the standard free energies of formation at 298.15 K of CuO, $Cu(OH)_2$, and $H_2O(g)$ from ref 60, which suggests that either the CuO is overstabilized or $Cu(OH)_2$ is destabilized in PBE+*U*+D3BJ. [c]Experimental values are −0.81 eV/Cu for CuO reduction with $(HCOOH)_2$ and −0.56 eV/Cu for Cu_2O oxidation with O_2. They were calculated using the standard free energies of formation at 298.15 K of CuO, Cu_2O, $CO_2(g)$, $H_2O(g)$, and $O_2(g)$ from ref 60, and $(HCOOH)_2$ from ref 66. [d]The free energy of formation of O(g) at 350 and 400 K were alternatively used in the calculation of the free energy of $O_2(g)$ at 353 and 403 K (see section 2.2 for the equation), which were taken from the NIST-JANAF database.[60]

HCOOH chemistry as a reductant

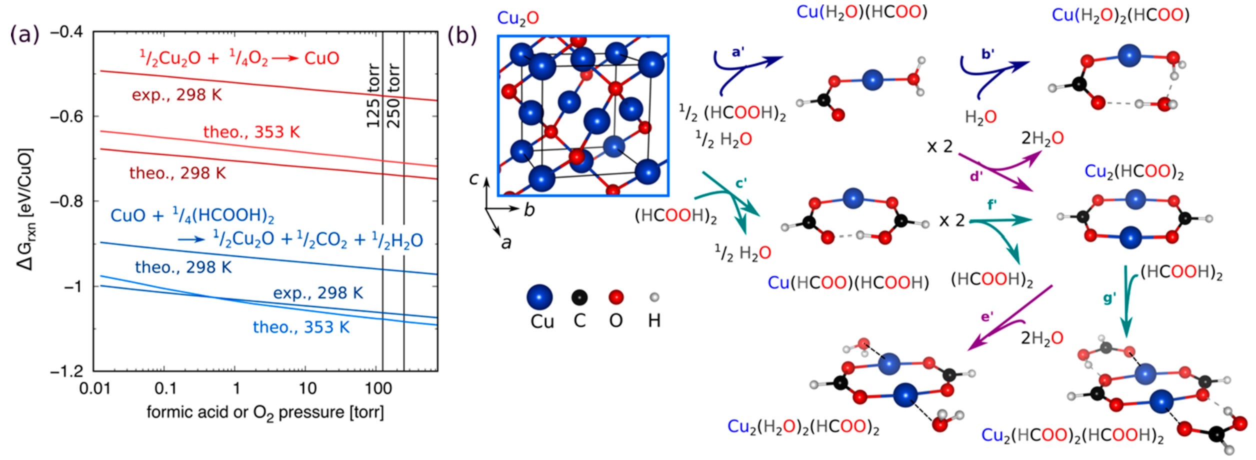

Figure 7. (a) Free energy of CuO reduction to Cu_2O, with $(HCOOH)_2$ as the reductant, and Cu_2O oxidation to CuO, with O_2 as the oxidant, as functions of the partial pressures of the reductant and oxidant molecules. Upper and lower bound total pressures of all HCOOH species ($(HCOOH)_n$): 250 and 125 Torr are marked, representing 100 and 50% $(HCOOH)_n$ in the $(HCOOH)_n$+N_2 gas stream at the total exposure pressure of 250 Torr, respectively. CO_2 and H_2O partial pressures are set to 0.08 Torr (1/10 of the vacuum base pressure). (b) DFT-predicted candidate gas-phase products from etching crystalline Cu_2O in the presence of formic acid and water vapor. Reactions are indexed from **a′** to **g′**. The product molecules are aquaformato (**a′** and **b′**) and formato(formic acid) (**c′**) complexes of Cu(I). Dinuclear diformato (**d′**) and diaquadiformato (**e′**) complexes are products, for example, of the dimerization of $Cu(H_2O)(HCOO)$. An alternative path for dimerization, relevant at low H_2O and high HCOOH conditions, is through Cu(HCOO)(HCOOH) (**f′**), which may be followed by coordination of two more HCOOH molecules forming $Cu_2(HCOO)_2(HCOOH)_2$ (**g′**).

reaction to −0.75 eV/CuO, an approximately −0.2 eV error. At very low O_2 partial pressure, e.g., 0.01 Torr, and at 353 K, this reaction remains very thermodynamically favorable even when accounting for the possible error in the prediction of the oxidation free energy (Figure 7a, red lines). Cu_2O thus will dominate only when the chamber is completely depleted of O_2. The relative rates of the reductive and oxidative reactions will dictate the relative amounts of Cu(II) and Cu(I) exposed for etching. From previous thermogravimetry coupled with quadrupole mass spectroscopy experiments, reduction of copper(II) oxide nanoparticles to copper(I) oxide with formic acid was found to occur between 220−250 °C (498−523 K), which is then followed by reduction to metallic Cu at *T* > 350 °C (623 K).[48] Temperature-programmed desorption (TPD) studies also found that the CO_2 desorption peak on Cu_2O film pre-exposed to HCOOH vapor at 300 K appears at around 545 K.[74] TPD experiments on copper surfaces, from metallic Cu to CuO, showed positive correlation between the HCOOH decomposition TPD peak temperature and degree of oxidation of the surface.[74] Lower temperature reduction of CuO and Cu_2O with HCOOH only occurs in the presence of a catalyst, e.g., Pt, which can facilitate the formation of H radicals from HCOOH at a lower temperature.[48,75] Reduction of CuO (and Cu_2O) with HCOOH thus is kinetically suppressed.

A possible combination of Cu(II) and Cu(I) is suggested in the Cu LMM Auger line XPS spectra post-etching (Figure S5). Below, we computationally explore the extent of participation of Cu(I) in the etching process and show that Cu(I) is harder to remove than Cu(II). At the O_2 plasma step, both the residual Cu(I) and re-exposed Cu(0) will be oxidized to Cu(II), which will facilitate the removal of Cu.

We performed a similar analysis on the possible etching products of Cu_2O (Figure 7b) with the formate ion and neutral molecules, namely, water and formic acid (Figure 7b). Cu(I) is a closed-shell d^{10} transition-metal ion and forms a linear coordination with two lattice O in the cubic Cu_2O crystal.[76] Much like in the solid, Cu(I) complexes were also found to prefer 2-fold coordination, e.g., aquaformato Cu(I) complex, $Cu(H_2O)(\kappa^1\text{-}HCOO)$ or simply $Cu(H_2O)(HCOO)$ (Figure 7b, reaction **a′**). The linear coordination in $Cu(H_2O)(HCOO)$ is found to be favored over a bent structure, although only by 0.08 eV at 298 K (Figure S9 and Table S5). $Cu(H_2O)(HCOO)$ was found to be unable to accommodate a second H_2O molecule as a third ligand and simply binds the second H_2O molecule via hydrogen bonding with the coordinated H_2O and $HCOO^-$ (reaction **b′**). The intramolecular hydrogen bonding in $Cu(H_2O)_2(HCOO)$ renders the second H_2O to be bound favorably (Table 1, reaction **b′**). Another monomer, the formato(formic acid) Cu(I) complex, $Cu(\kappa^1\text{-}HCOO)(\kappa^1\text{-}HCOOH)$ or Cu(HCOO)(HCOOH), exhibits interligand hydrogen bonding (reaction **c′**), which slightly bends the molecule. When this interligand hydrogen bonding breaks, as in a staggered ligand conformation, which

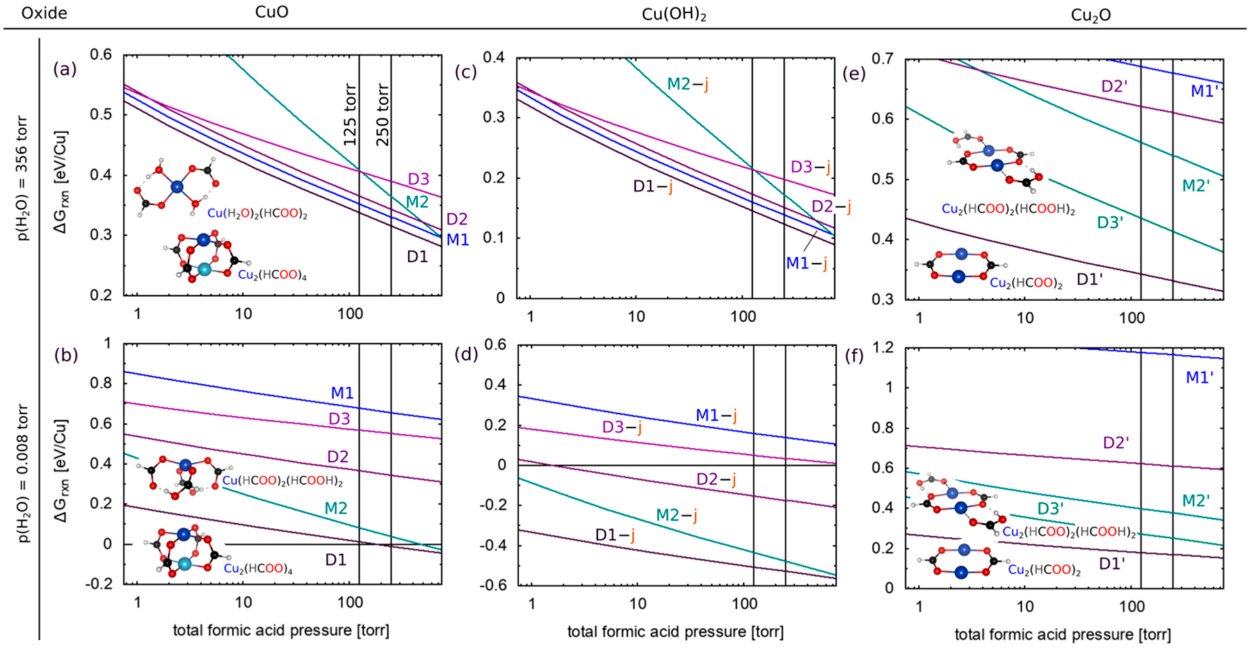

Figure 8. (a,b) and (c,d) Reaction free energy (eV/Cu) to form the most stable Cu(II) monomers: $Cu(H_2O)_2(HCOO)_2$ and $Cu(HCOO)_2(HCOOH)_2$ (reactions M1 and M2), and dimers $Cu_2(HCOO)_4$, $Cu_2(H_2O)_2(HCOO)_4$, and $Cu_2(H_2O)_2(HCOO)_3(OH)$ (reactions Dm, m = 1−3), from CuO and $Cu(OH)_2$, respectively, as a function of the total pressure of formic acid species (logarithmic scale) at 353 K (80 °C), at two different ambient water vapor pressures (356 and 8.0×10^{-3} Torr). For (c,d), j is the free energy to form $Cu(OH)_2$ from CuO (Table 1). (e,f) A similar plot for the Cu(I) complexes. The most stable molecules are, namely, monomers $Cu(H_2O)(HCOO)$ and $Cu(HCOO)(HCOOH)$ (reactions M1′ and M2′) and dimers $Cu_2(HCOO)_2$, $Cu_2(H_2O)_2(HCOO)_2$, and $Cu(HCOO)_2(HCOOH)_2$ (reactions Dm′, m = 1−3). In all plots, a low Cu complex pressure of 8.0×10^{-2} Torr was assumed (1/10 of the vacuum base pressure). Insets show the two lowest-energy structures for each water vapor pressure condition. Upper and lower bound total pressures of all HCOOH species ($(HCOOH)_n$): 250 and 125 Torr are marked, representing 100 and 50% $(HCOOH)_n$ in the $(HCOOH)_n$+N_2 gas stream at the total exposure pressure of 250 Torr, respectively. The plots were constructed from the standard reaction free energies in Table 1. See also Table 1 for the definition of the reaction indices.

recovers a perfectly linear configuration (Figure S9 and Table S5), its energy increases by 0.60 eV at 298 K.

Finally, we also explore the dimerization of Cu(I). Much like in Cu(II), the dimeric Cu(I) formato complex, $Cu_2(\mu\text{-}HCOO)_2$, may form by dehydration of the monomeric aquaformato complexes ($Cu(H_2O)(HCOO)$ or $Cu(H_2O)_2(HCOO)$). Reaction **d′** in Figure 7b shows the dimerization from $Cu(H_2O)(HCOO)$ (−0.85 eV/Cu at 353 K, Table 1). A dimer can also form from $Cu(H_2O)(HCOO)$ without losing water to form instead $Cu_2(H_2O)_2(\mu\text{-}HCOO)_2$, corresponding to the sum of reactions **d′** and **e′** in Figure 7b (−0.68 eV/Cu at 353 K, Table 1). Under water-lean conditions, the formation of $Cu_2(\mu\text{-}HCOO)_2$ may be better facilitated by the dimerization of $Cu(HCOO)(HCOOH)$ represented by reaction **f′**, Figure 7b (−0.33 eV/Cu at 353 K, Table 1). At HCOOH-rich conditions, additional HCOOH may coordinate with $Cu_2(\mu\text{-}HCOO)_2$ (reaction **g′**,Figure 7b) to form $Cu_2(\mu\text{-}HCOO)_2(\kappa^1\text{-}HCOOH)_2$ or simply $Cu_2(HCOO)_2(HCOOH)_2$. Unlike in Cu(II), $Cu_2(HCOO)_2(HCOOH)_2$ is incapable of forming a paddlewheel structure. This is largely due to the preference of Cu(I) to remain in a 2-fold coordinated environment. In both $Cu_2(H_2O)_2(HCOO)_2$ and $Cu_2(HCOO)_2(HCOOH)_2$, the third ligand around a Cu ion is bound much more weakly and the formation of a fourth dative bond, e.g., in $Cu_2(\mu\text{-}HCOO)_2(\mu\text{-}HCOOH)_2$, is outright unfavorable.

3.4.3. *Predicted Thermodynamics under Experimental Conditions.*

Although the reactions are shown in a particular sequence in Figure 6 for Cu(II) and Figure 7b for Cu(I), the formation of these complexes need not proceed in the same manner presented. Therefore, Table 1 presents also the standard reaction free energies to form (from CuO, $(HCOOH)_2$, and H_2O) the most stable monomers $Cu(H_2O)_2(HCOO)_2$ and $Cu(HCOO)_2(HCOOH)_2$ (reactions Mm, m = 1 and 2) and dimers $Cu_2(HCOO)_4$, $Cu_2(H_2O)_2(HCOO)_4$, and $Cu_2(H_2O)_2(HCOO)_3(OH)$ (reactions Dm, m = 1, 2, and 3). Table 1 also presents the standard reaction free energies to form (from Cu_2O, $(HCOOH)_2$, and H_2O) the most stable monomers $Cu(H_2O)_2(HCOO)$ and $Cu(HCOO)(HCOOH)$ (reactions Mm′, m = 1 and 2) and dimers $Cu(HCOO)_2$, $Cu_2(H_2O)_2(HCOO)_2$, and $Cu_2(HCOO)_2(HCOOH)_2$ (reactions Dm′, m = 1, 2, and 3). Henceforth, the free energies of these reactions are referred to as "formation" free energies (in contrast to the regular definition of a formation free energy, which uses the pure standard forms of the constituent elements as references). These standard formation Gibb's free energies then were extrapolated to experimental pressures of the gaseous reactants and products.

To calculate the partial pressure of $(HCOOH)_2$ given the total pressure of all the formic acid species, the calculated dimerization free energy for HCOOH(g) (Supporting Information, methods section II) was used. The total chamber pressure is the result of unreacted HCOOH and the carrier gas N_2 (both deemed to be the majority gases), the product Cu complex, and H_2O (initially present or as a product of the neutralization reaction). 8.0×10^{-2} Torr or 1/10 of the vacuum base pressure (0.8 Torr) was used as the upper bound for the complex (vacuum condition is achieved pre-etching).

As for the H_2O vapor pressure, two extreme cases were defined: (1) 356 Torr and (2) 1/100 of the vacuum chamber base pressure, 8.0×10^{-3} Torr. Case (1) occurs when the vacuum condition is broken and never recovered (vacuum is broken between O_2 plasma exposure and HCOOH etching, and the saturation pressure of water at the experimental temperature of 353 K (80 °C) is 356 Torr).[77] Case (2) is relevant during etching (performed at 250 Torr) where the vacuum condition is recovered prior (base pressure of 0.8 Torr) and the chamber is subsequently filled with HCOOH/N_2 at 250 Torr, displacing more H_2O out of the reaction vessel ("dry" condition). The latter is the more relevant case in the current experiment, whereas the former is shown for comparison as a hypothetical case. The partial-pressure dependence of the reaction free energies is described in Supporting Information, methods section III. Below, we predict that due to the difference in water content in the complexes described above, the monomer and dimers may prevail at the higher water vapor pressure conditions. For Cu(II), under water condition (1), $Cu(H_2O)_2(HCOO)_2$ is the most preferred monomer while $Cu_2(\mu\text{-HCOO})_4$ is favored among the three dimers, and overall. Under water condition (2) or the "dry" condition, the dehydrated $Cu_2(\mu\text{-HCOO})_4$ dominates and the monomeric $Cu(HCOO)_2(HCOOH)_2$ is favored over $Cu(H_2O)_2(HCOO)_2$, where the latter is significantly destabilized. For Cu(I), $Cu_2(\mu\text{-HCOO})_2$ prevails in both water conditions and is more difficult to form than $Cu_2(\mu\text{-HCOO})_4$ from their respective oxides of the same Cu oxidation state.

Figure 8a shows the reaction free energies for reactions M1, M2 and D1–D3 (Table 1) as a function of the total pressure of all the formic acid species ($(HCOOH)_n$), which can be directly measured or estimated from the experiment. Given a total etchant ($(HCOOH)_n$+N_2) pressure of 250 Torr, an upper bound of 250 Torr and a lower bound 125 Torr were defined for the partial pressure of $(HCOOH)_n$. These pressures are marked in the plots in Figure 8. It becomes apparent from the plots that the monomer $Cu(H_2O)_2(HCOO)_2$ and dimers are most likely to form competitively during etching in the presence of ambient water vapor, albeit with $Cu_2(\mu\text{-HCOO})_4$ slightly more favored with a slightly positive formation free energy of 0.32–0.34 eV/Cu at relevant $(HCOOH)_n$ pressures. However, under the "dry" condition, only the water-free dimer $Cu_2(\mu\text{-HCOO})_4$ prevails, with nearly zero formation free energy that is between −0.01 and +0.01 eV/Cu. Thus, recovery of the vacuum prior to etching is imperative to drive the etching to spontaneity, because it deprives the chamber of one of the neutralization products: water vapor. The formation of $Cu(H_2O)_2(HCOO)_2$ under this condition is highly unfavorable; however, the thermodynamics of $Cu(HCOO)_2(HCOOH)_2$ formation is enhanced. $Cu(HCOO)_2(HCOOH)_2$ then may act as a more favorable intermediate for the formation of $Cu_2(\mu\text{-HCOO})_4$. The dimerization, which releases $(HCOOH)_2$, is between −0.07 and −0.05 eV/Cu from 125 to 250 Torr total formic acid at 353 K (these energies are independent of the partial pressure of H_2O). $Cu_2(\mu\text{-HCOO})_4$ can also form from the reaction of $Cu(HCOO)_2(HCOOH)_2$ with a unit of CuO(s):

$$Cu(HCOO)_2(HCOOH)_2 + CuO(s) \rightarrow Cu_2(HCOO)_4 + H_2O(g)$$

In such a reaction, the two protons from the two HCOOH ligands react with a lattice O to form H_2O, and the resulting four free carboxyl O anions anchor onto and extract a Cu(II) ion. This pathway is also spontaneous at 0.008 Torr H_2O, with a reaction free energy of −0.06 eV/dimer or −0.03 eV/Cu at 353 K (independent of the partial pressure of $(HCOOH)_2$) and is thus competitive with the dimerization reaction described above. Note that this step is unfavorable at 356 Torr H_2O (+0.27 eV at 353 K).

Because the experiment demonstrated the existence of $Cu(OH)_2$, the same plots using $Cu(OH)_2$ instead of CuO as reactant were obtained. This is easily achieved by subtracting the water-vapor-pressure-dependent free energy to form $Cu(OH)_2$ from CuO and $H_2O(g)$ (reaction **j** in Figure 6 and Table 1) from the free energies in Figure 8a,b. The resulting plots appear in Figure 8c,d. Because **j** has a positive free energy (especially at very low H_2O partial pressures), the formation energies are more negative than in the case of CuO. Despite the energy shift, the relative stability of the complexes is maintained. However, it is known experimentally that under low humidity conditions for oxidation, little or no $Cu(OH)_2$ forms. The relevant reactions are therefore those that involve CuO as the reactant.

As for Cu(I) complexation, Figure 8e,f depicts the formation free energy versus total formic acid pressure of the notable monomer and dimer Cu(I) complexes: M1′, M2′ and D1′–D3′ (Table 1). In both water-rich and -deprived conditions, the dimer $Cu_2(\mu\text{-HCOO})_2$ (D1′) is the most favorable to form. Another dimer, $Cu_2(\mu\text{-HCOO})_2(HCOOH)_2$ (D3′), is the second most favorable species. The free energy of formation of $Cu_2(\mu\text{-HCOO})_2$ from Cu_2O ranges from 0.33 to 0.34 eV/Cu at 356 Torr H_2O and 353 K, which slightly improves to 0.17–0.18 eV/Cu at 0.008 Torr H_2O. Addition of two HCOOH to form D3′ slightly increases the free energy of this dimer by ~0.1 eV/Cu. Cu(HCOO)(HCOOH) (M2′) on the other hand is ~0.2 eV/Cu higher in energy than D1′. Cu(HCOO)(HCOOH), therefore, cannot facilitate the formation of the most stable dimer.

Etching of Cu(I) through complexation is thermodynamically less favorable than Cu(II) by ~0.2 eV/Cu, and unlike in Cu(II), a Cu(I) monomer that is energetically adjacent to the most stable Cu(I) dimer does not exist. Therefore, Cu(II) is expected to be the species that may be etched by HCOOH, which highlights the importance of the oxidation half-cycle with plasma O_2, to oxidize the newly exposed Cu after etching and any Cu(I) that may form.

The etching of oxidized Cu mediated by HCOOH vapor may be regarded as rather "inefficient" considering it proceeds only a few nm per cycle (2.4 nm/cycle, Figure 4a) with a 5 min exposure to HCOOH per cycle, but desirable because it enables a nanometer-resolved etch rate. This "inefficiency" is reflected in the predicted nearly zero etching free energy of Cu(II) through complexation under experimental conditions (Figure 8b). Atomic resolution thus is achieved by the complexation reactions that are at or near equilibrium.

3.4.4. Possible Avenues for Product Detection. The fate of $Cu_2(\mu\text{-HCOO})_4$ is unknown in the experiment. It is likely that it may collect on the colder part of the vacuum system, perhaps forming precipitates. Cu(II), formate, and water are known to form a monoclinic copper formate tetrahydrate crystal: $Cu(HCOO)_2\cdot(H_2O)_4$, composed of alternating layers of $Cu(HCOO)_2$ and $(H_2O)_4$ along its *c*-axis.[78,79] It is thus more likely to form this compound at higher water vapor conditions at lower temperatures, which perhaps can be an avenue for future experimental detection of the etching products.

4. SUMMARY AND CONCLUSIONS

Atomic layer etching of Cu was achieved by using an O_2 plasma as the controlled oxidant and HCOOH vapor as the self-limiting etchant. This procedure was cycled until the desired amount of Cu was etched. From first-principles DFT $+U$ with van der Waals correction simulations, it was shown that CuO can be etched by HCOOH, by first neutralizing the oxide and then forming a complex with the $HCOO^-$ ions. Under relevant experimental pressures (125 to 250 Torr formic acid etchant, with the partial pressures of the complex and water 1/10 and 1/100 of the vacuum base pressure of the reactor, i.e., 0.8 Torr, respectively), the DFT analysis predicted that the water-free dimeric gas-phase product $Cu_2(\mu\text{-}HCOO)_4$ is most likely to form under water-deprived conditions, highlighting that re-establishing vacuum prior to acid etching is critical. The formation of Cu_2O from CuO, where HCOOH acts as a reductant, was also considered as a reaction prior to complexation (reductive etching). However, Cu(I) etching from Cu_2O was found to be less thermodynamically favorable than Cu(II) etching from CuO. To conclude, etching the oxide presents a clear advantage over directly etching metals. The use of vapor phase over solution phase of the acidic etchant also provided control over the etching selectivity and anisotropy.

■ ASSOCIATED CONTENT

Supporting Information

The Supporting Information is available free of charge at https://pubs.acs.org/doi/10.1021/acs.jpcc.0c08932.

Supplementary methods, optimized crystal structures and phonon densities of states of bulk CuO, $Cu(OH)_2$, and Cu_2O, SEM images of as-deposited Cu, after oxidation, and after HCOOH etching at different etching times, Cu-LMM Auger line XPS and Wagner plot for the different Cu species, HCOOH monomer and dimer structures, alternative structures of some of the monomeric Cu(II)- and Cu(I)-(formato, formic acid) complexes, structures and free energies of formation of the Cu(II)-aquahydroxo complexes relative to $Cu(OH)_2$ and $H_2O(g)$, data tables of the optimized lattice parameters, k-point sampling, and relative energies of the different magnetic ordering for CuO and $Cu(OH)_2$, data tables summarizing the enthalpic and entropic energies of the solids (vibrational) and gaseous molecules (vibrational, rotational, and translational), data table showing the relative energies of the different magnetic orderings for the Cu(II) dimer complexes (PDF)

Optimized-atomic-structure files of the ground-state bulk crystals (VASP format) and isolated molecules (xyz format) (ZIP)

■ AUTHOR INFORMATION

Corresponding Authors

Emily A. Carter − *Department of Chemical and Biomolecular Engineering and Office of the Chancellor, University of California, Los Angeles, Los Angeles, California 90095, United States; Department of Mechanical and Aerospace Engineering, Princeton University, Princeton, New Jersey 08544-5263, United States;* orcid.org/0000-0001-7330-7554; Email: eac@ucla.edu, eac@princeton.edu

Jane P. Chang − *Department of Chemical and Biomolecular Engineering and Department of Materials Science and Engineering, University of California, Los Angeles, Los Angeles, California 90095, United States;* orcid.org/0000-0001-8482-5744; Email: jpchang@ucla.edu

Authors

Ryan Sheil − *Department of Chemical and Biomolecular Engineering, University of California, Los Angeles, Los Angeles, California 90095, United States*

J. Mark P. Martirez − *Department of Chemical and Biomolecular Engineering, University of California, Los Angeles, Los Angeles, California 90095, United States;* orcid.org/0000-0003-0566-6605

Xia Sang − *Department of Materials Science and Engineering, University of California, Los Angeles, Los Angeles, California 90095, United States*

Complete contact information is available at: https://pubs.acs.org/10.1021/acs.jpcc.0c08932

Author Contributions

$^\perp$R.S. and J.M.P.M. contributed equally to this work.

Notes

The authors declare no competing financial interest.

■ ACKNOWLEDGMENTS

E.A.C. acknowledges financial support from UCLA for this project. This work used computational and storage services associated with the Hoffman2 Shared Cluster provided by UCLA Institute for Digital Research and Education's Research Technology Group. J.P.C. acknowledges the support from Lam Research, the Center for Design-Enabled Nanofabrication (C-DEN) Program, and National Science Foundation (1805112).

■ REFERENCES

(1) Edelstein, D.; Heidenreich, J.; Goldblatt, R.; Cote, W.; Uzoh, C.; Lustig, N.; Roper, P.; McDevitt, T.; Motsiff, W.; Simon, A. Full copper wiring in a sub-0.25 μm CMOS ULSI technology. *International Electron Devices Meeting. IEDM Technical Digest* **1997**, 773−776.

(2) Rosenberg, R.; Edelstein, D.; Hu, C.-K.; Rodbell, K. Copper Metallization for High Performance Silicon Technology. *Annu. Rev. Mater. Sci.* **2000**, *30*, 229−262.

(3) Cheung, R.; Lopatin, S. Method for Filling a Dual Damascene Opening Having High Aspect Ratio to Minimize Electromigration Failure. US6245670B1, 2001.

(4) Kodera, M.; Uekusa, S.-I.; Nagano, H.; Tokushige, K.; Shima, S.; Fukunaga, A.; Mochizuki, Y.; Fukuda, A.; Hiyama, H.; Tsujimura, M.; Nagai, H.; Maekawa, K. Stress Corrosion Cracking of Cu Interconnects During CMP with a Cu/Porous Low-K Structure. *J. Electrochem. Soc.* **2005**, *152*, G506−G510.

(5) Kulkarni, N. S.; DeHoff, R. T. Application of Volatility Diagrams for Low Temperature, Dry Etching, and Planarization of Copper. *J. Electrochem. Soc.* **2002**, *149*, G620−G632.

(6) Ohmi, H.; Sato, J.; Shirasu, Y.; Hirano, T.; Kakiuchi, H.; Yasutake, K. Significant Improvement of Copper Dry Etching Property of a High-Pressure Hydrogen-Based Plasma by Nitrogen Gas Addition. *ACS Omega* **2019**, *4*, 4360−4366.

(7) Kuo, Y.; Lee, S. Room-Temperature Copper Etching Based on a Plasma-Copper Reaction. *Appl. Phys. Lett.* **2001**, *78*, 1002−1004.

(8) Wu, F.; Levitin, G.; Hess, D. W. Patterning of Cu Films by a Two-Step Plasma Etching Process at Low Temperature. *J. Electrochem. Soc.* **2010**, *157*, H474−H478.

(9) Edelstein, D. C. 20 Years of Cu BEOL in Manufacturing, and Its Future Prospects. *2017 IEEE International Electron Devices Meeting (IEDM)* **2017**, 14.1.1−14.1.4.

(10) Yeoh, A.; Madhavan, A.; Kybert, N.; Anand, S.; Shin, J.; Asoro, M.; Samarajeewa, S.; Steigerwald, J.; Ganpule, C.; Buehler, M. Interconnect Stack Using Self-Aligned Quad and Double Patterning for 10nm High Volume Manufacturing. *2018 IEEE International Interconnect Technology Conference- IITC* **2018**, 144−147.

(11) Carver, C. T.; Plombon, J. J.; Romero, P. E.; Suri, S.; Tronic, T. A.; Turkot, R. B. Atomic Layer Etching: An Industry Perspective. *ECS J. Solid State Sci. Technol.* **2015**, *4*, N5005−N5009.

(12) Bard, A. *Standard Potentials in Aqueous Solution*; Routledge, 2017.

(13) Gordon, P. G.; Kurek, A.; Barry, S. T. Trends in Copper Precursor Development for CVD and ALD Applications. *ECS J. Solid State Sci. Technol.* **2015**, *4*, N3188−N3197.

(14) Sauer, J. Molecular Models in Ab Initio Studies of Solids and Surfaces: From Ionic Crystals and Semiconductors to Catalysts. *Chem. Rev.* **1989**, *89*, 199−255.

(15) Carter, E. A. Challenges in Modeling Materials Properties without Experimental Input. *Science* **2008**, *321*, 800−803.

(16) Cramer, C. J.; Truhlar, D. G. Density Functional Theory for Transition Metals and Transition Metal Chemistry. *Phys. Chem. Chem. Phys.* **2009**, *11*, 10757−10816.

(17) Dieterich, J. M.; Carter, E. A. Quantum Solutions for a Sustainable Energy Future. *Nat. Rev. Chem.* **2017**, *1*, 0032.

(18) Maurer, R. J.; Freysoldt, C.; Reilly, A. M.; Brandenburg, J. G.; Hofmann, O. T.; Bjorkman, T.; Lebegue, S.; Tkatchenko, A. Advances in Density-Functional Calculations for Materials Modeling. *Annu. Rev. Mater. Res.* **2019**, *49*, 1−30.

(19) Walsh, A.; Chen, S. Y.; Wei, S. H.; Gong, X. G. Kesterite Thin-Film Solar Cells: Advances in Materials Modelling of Cu_2ZnSnS_4. *Adv. Energy Mater.* **2012**, *2*, 400−409.

(20) Xiao, Z. W.; Yan, Y. F. Progress in Theoretical Study of Metal Halide Perovskite Solar Cell Materials. *Adv. Energy Mater.* **2017**, *7*, 1701136.

(21) Sai Gautam, G.; Senftle, T. P.; Alidoust, N.; Carter, E. A. Novel Solar Cell Materials: Insights from First-Principles. *J. Phys. Chem. C* **2018**, *122*, 27107−27126.

(22) Nørskov, J. K.; Bligaard, T.; Rossmeisl, J.; Christensen, C. H. Towards the Computational Design of Solid Catalysts. *Nat. Chem.* **2009**, *1*, 37−46.

(23) Liao, P. L.; Carter, E. A. New Concepts and Modeling Strategies to Design and Evaluate Photo-Electro-Catalysts Based on Transition Metal Oxides. *Chem. Soc. Rev.* **2013**, *42*, 2401−2422.

(24) Pham, T. A.; Ping, Y.; Galli, G. Modelling Heterogeneous Interfaces for Solar Water Splitting. *Nat. Mater.* **2017**, *16*, 401−408.

(25) Xu, S. Z.; Carter, E. A. Theoretical Insights into Heterogeneous (Photo)Electrochemical CO_2 Reduction. *Chem. Rev.* **2019**, *119*, 6631−6669.

(26) Govind Rajan, A.; Martirez, J. M. P.; Carter, E. A. Why Do We Use the Materials and Operating Conditions We Use for Heterogeneous (Photo)Electrochemical Water Splitting? *ACS Catal.* **2020**, *10*, 11177−11234.

(27) Martirez, J. M. P.; Bao, J. L.; Carter, E. A. First-Principles Insights into Plasmon-Induced Catalysis. *Annu. Rev. Phys. Chem.* **2021**, *72*, DOI: 10.1146/annurev-physchem-061020-053501

(28) Meng, Y. S.; Arroyo-de Dompablo, M. E. First Principles Computational Materials Design for Energy Storage Materials in Lithium Ion Batteries. *Energy Environ. Sci.* **2009**, *2*, 589−609.

(29) Ceder, G. Opportunities and Challenges for First-Principles Materials Design and Applications to Li Battery Materials. *MRS Bull.* **2010**, *35*, 693−701.

(30) Radeke, M. R.; Carter, E. A. Ab Initio Dynamics of Surface Chemistry. *Annu. Rev. Phys. Chem.* **1997**, *48*, 243−270.

(31) Reuter, K.; Stampf, C.; Scheffler, M. Ab Initio Atomistic Thermodynamics and Statistical Mechanics of Surface Properties and Functions. In *Handbook of Materials Modeling*; Yip, S., Ed.; Springer: Dordrecht, The Netherlands, 2005; pp 149−194.

(32) Marino, K. A.; Hinnemann, B.; Carter, E. A. Atomic-Scale Insight and Design Principles for Turbine Engine Thermal Barrier Coatings from Theory. *Proc. Natl. Acad. Sci. U. S. A.* **2011**, *108*, 5480−5487.

(33) Ikeda, Y.; Grabowski, B.; Kormann, F. Ab Initio Phase Stabilities and Mechanical Properties of Multicomponent Alloys: A Comprehensive Review for High Entropy Alloys and Compositionally Complex Alloys. *Mater. Charact.* **2019**, *147*, 464−511.

(34) Cavallotti, C.; Gupta, V.; Sieber, C.; Jensen, K. F. Dissociation Reactions of Cu^I(Hfac)L Compounds Relevant to the Chemical Vapor Deposition of Copper. *Phys. Chem. Chem. Phys.* **2003**, *5*, 2818−2827.

(35) Maimaiti, Y.; Elliott, S. D. Kinetics and Coverage Dependent Reaction Mechanisms of the Copper Atomic Layer Deposition from Copper Dimethylamino-2-Propoxide and Diethylzinc. *Chem. Mater.* **2016**, *28*, 6282−6295.

(36) Kondati Natarajan, S.; Elliott, S. D. Modeling the Chemical Mechanism of the Thermal Atomic Layer Etch of Aluminum Oxide: A Density Functional Theory Study of Reactions During HF Exposure. *Chem. Mater.* **2018**, *30*, 5912−5922.

(37) Longo, R. C.; Ranjan, A.; Ventzek, P. L. Density Functional Theory Study of Oxygen Adsorption on Polymer Surfaces for Atomic Layer Etching: Implications for Semiconductor Device Fabrication. *ACS Appl. Nano Mater.* **2020**, *3*, 5189−5202.

(38) Altieri, N. D.; Chen, J. K.-C.; Minardi, L.; Chang, J. P. Plasma-Surface Interactions at the Atomic Scale for Patterning Metals. *J. Vac. Sci. Technol., A* **2017**, *35*, 05C203.

(39) Gong, Y.; Venkatraman, K.; Akolkar, R. Communication—Electrochemical Atomic Layer Etching of Copper. *J. Electrochem. Soc.* **2018**, *165*, D282−D284.

(40) Mohimi, E.; Chu, X. I.; Trinh, B. B.; Babar, S.; Girolami, G. S.; Abelson, J. R. Thermal Atomic Layer Etching of Copper by Sequential Steps Involving Oxidation and Exposure to Hexafluoroacetylacetone. *ECS J. Solid State Sci. Technol.* **2018**, *7*, P491−P495.

(41) Waechtler, T.; et al. ALD-Grown Seed Layers for Electrochemical Copper Deposition Integrated with Different Diffusion Barrier Systems. *Microelectron. Eng.* **2011**, *88*, 684−689.

(42) Norman, J. A. T.; Perez, M.; Schulz, S. E.; Waechtler, T. New Precursors for CVD Copper Metallization. *Microelectron. Eng.* **2008**, *85*, 2159−2163.

(43) Knisley, T. J.; Ariyasena, T. C.; Sajavaara, T.; Saly, M. J.; Winter, C. H. Low Temperature Growth of High Purity, Low Resistivity Copper Films by Atomic Layer Deposition. *Chem. Mater.* **2011**, *23*, 4417−4419.

(44) Polyakov, M. S.; Badalyan, A. M.; Kaichev, V. V.; Igumenov, I. K. Thermal- and Plasma-Enhanced Copper Film Deposition Via a Combined Synthesis-Transport CVD Technique. *Chem. Vap. Deposition* **2014**, *20*, 170−176.

(45) Song, H.; Norman, J. A. T.; Shimogaki, Y. Evaluation of a Novel Unfluorinated Copper Precursor for Chemical Vapor Deposition. *Microelectron. Eng.* **2010**, *87*, 249−253.

(46) Iglesia, E.; Boudart, M. Decomposition of Formic Acid on Copper, Nickel, and Copper-Nickel Alloys: II. Catalytic and Temperature-Programmed Decomposition of Formic Acid on $CuSiO_2$, $CuAl_2O_3$, and Cu Powder. *J. Catal.* **1983**, *81*, 214−223.

(47) Chou, P.-W.; Song, J.-M.; Xie, Z.-Y.; Akaike, M.; Suga, T.; Fujino, M.; Lin, J.-Y. Low Temperature De-Oxidation for Copper Surface by Catalyzed Formic Acid Vapor. *Appl. Surf. Sci.* **2018**, *456*, 890−898.

(48) Fujino, M.; Akaike, M.; Matsuoka, N.; Suga, T. Reduction Reaction Analysis of Nanoparticle Copper Oxide for Copper Direct Bonding Using Formic Acid. *Jpn. J. Appl. Phys.* **2017**, *56*, 04CC01.

(49) Blöchl, P. E. Projector Augmented-Wave Method. *Phys. Rev. B: Condens. Matter Mater. Phys.* **1994**, *50*, 17953−17979.

(50) Kresse, G.; Furthmuller, J. Efficient Iterative Schemes for Ab Initio Total-Energy Calculations Using a Plane-Wave Basis Set. *Phys. Rev. B: Condens. Matter Mater. Phys.* **1996**, *54*, 11169−11186.

(51) Perdew, J. P.; Burke, K.; Ernzerhof, M. Generalized Gradient Approximation Made Simple. *Phys. Rev. Lett.* **1996**, *77*, 3865−3868.

(52) Dudarev, S. L.; Botton, G. A.; Savrasov, S. Y.; Humphreys, C. J.; Sutton, A. P. Electron-Energy-Loss Spectra and the Structural Stability of Nickel Oxide: An LSDA+U Study. *Phys. Rev. B: Condens. Matter Mater. Phys.* **1998**, *57*, 1505−1509.

(53) Yu, K.; Carter, E. A. Communication: Comparing Ab Initio Methods of Obtaining Effective U Parameters for Closed-Shell Materials. *J. Chem. Phys.* **2014**, *140*, 121105.

(54) Grimme, S.; Antony, J.; Ehrlich, S.; Krieg, H. A Consistent and Accurate Ab Initio Parametrization of Density Functional Dispersion Correction (DFT-D) for the 94 Elements H-Pu. *J. Chem. Phys.* **2010**, *132*, 154104.

(55) Grimme, S.; Ehrlich, S.; Goerigk, L. Effect of the Damping Function in Dispersion Corrected Density Functional Theory. *J. Comput. Chem.* **2011**, *32*, 1456−1465.

(56) Togo, A.; Tanaka, I. First Principles Phonon Calculations in Materials Science. *Scr. Mater.* **2015**, *108*, 1−5.

(57) Makov, G.; Payne, M. C. Periodic Boundary Conditions in Ab-Initio Calculations. *Phys. Rev. B: Condens. Matter Mater. Phys.* **1995**, *51*, 4014−4022.

(58) Neugebauer, J.; Scheffler, M. Adsorbate-Substrate and Adsorbate-Adsorbate Interactions of Na and K Adlayers on Al(111). *Phys. Rev. B: Condens. Matter Mater. Phys.* **1992**, *46*, 16067−16080.

(59) Chen, Z.; Martirez, J. M. P.; Zahl, P.; Carter, E. A.; Koel, B. E. Self-Assembling of Formic Acid on the Partially Oxidized $p(2 \times 1)$ Cu(110) Surface Reconstruction at Low Coverages. *J. Chem. Phys.* **2019**, *150*, 041720.

(60) Chase, M. W.; Davies, C. A.; Downey, J. R.; Frurip, D. J.; McDonald, R. A.; Syverud, A. N. *NIST-JANAF Thermochemical Tables 1985*; National Institute of Standards and Technology: Gaithersburg, MD, 1986; Vols. *1*−*2*.

(61) Biesinger, M. C. Advanced Analysis of Copper X-Ray Photoelectron Spectra. *Surf. Interface Anal.* **2017**, *49*, 1325−1334.

(62) Chu, Y.; Robinson, I.; Gewirth, A. A. Comparison of Aqueous and Native Oxide Formation on Cu(111). *J. Chem. Phys.* **1999**, *110*, 5952−5959.

(63) Yang, B. X.; Tranquada, J. M.; Shirane, G. Neutron-Scattering Studies of the Magnetic-Structure of Cupric Oxide. *Phys. Rev. B: Condens. Matter Mater. Phys.* **1988**, *38*, 174−178.

(64) Jin, G. X.; Cao, K.; Guo, G. C.; He, L. X. Origin of Ferroelectricity in High-T-C Magnetic Ferroelectric CuO. *Phys. Rev. Lett.* **2012**, *108*, 187205.

(65) Hietala, J.; Vuori, A.; Johnsson, P.; Pollari, I.; Reutemann, W.; Kieczka, H. Formic Acid. In *Ullmann's Encyclopedia of Industrial Chemistry*; Wiley-VCH Verlag GmbH & Co. KGaA, 2016; pp 1−22.

(66) Green, J. H. S. Thermodynamic Properties of Organic Oxygen Compounds. *Q. Rev., Chem. Soc.* **1961**, *15*, 125−152.

(67) Miessler, G. L.; Tarr, D. A. *Inorganic Chemistry*, 4th ed.; Pearson Prentice Hall, 2011.

(68) Patmore, N. J. Recent Developments in the Chemistry of Metal-Metal Multiply Bonded Paddlewheel Compounds. *Organo. Chem.* **2010**, *36*, 77−92.

(69) Chui, S. S.-Y.; Lo, S. M.-F.; Charmant, J. P. H.; Orpen, A. G.; Williams, I. D. A Chemically Functionalizable Nanoporous Material $[Cu_3(TMA)_2(H_2O)_3]_n$. *Science* **1999**, *283*, 1148−1150.

(70) Rungtaweevoranit, B.; Diercks, C. S.; Kalmutzki, M. J.; Yaghi, O. M. Spiers Memorial Lecture: Progress and Prospects of Reticular Chemistry. *Faraday Discuss.* **2017**, *201*, 9−45.

(71) Vanniekerk, J. N.; Schoening, F. R. L. X-Ray Evidence for Metal-to-Metal Bonds in Cupric and Chromous Acetate. *Nature* **1953**, *171*, 36−37.

(72) Graddon, D. P. The Dimerization of Cupric Propionate in Chloroform Solution. *J. Inorg. Nucl. Chem.* **1959**, *11*, 337−342.

(73) Pascher, T. F.; Ončák, M.; van der Linde, C.; Beyer, M. K. Decomposition of Copper Formate Clusters: Insight into Elementary Steps of Calcination and Carbon Dioxide Activation. *ChemistryOpen* **2019**, *8*, 1453−1459.

(74) Poulston, S.; Rowbotham, E.; Stone, P.; Parlett, P.; Bowker, M. Temperature-Programmed Desorption Studies of Methanol and Formic Acid Decomposition on Copper Oxide Surfaces. *Catal. Lett.* **1998**, *52*, 63−67.

(75) Chou, P. W.; Song, J. M.; Xie, Z. Y.; Akaike, M.; Suga, T.; Fujino, M.; Lin, J. Y. Low Temperature De-Oxidation for Copper Surface by Catalyzed Formic Acid Vapor. *Appl. Surf. Sci.* **2018**, *456*, 890−898.

(76) Kirfel, A.; Eichhorn, K. Accurate Structure-Analysis with Synchrotron Radiation - the Electron-Density in Al_2O_3 and Cu_2O. *Acta Crystallogr., Sect. A: Found. Crystallogr.* **1990**, *46*, 271−284.

(77) Thermophysical Properties of Fluid Systems. In *NIST Chemistry WebBook, SRD 69*, 2018. https://webbook.nist.gov/chemistry/fluid/.

(78) Omura, T.; Moriyoshi, C.; Itoh, K.; Ikeda, S.; Fukazawa, H. Structural Change of $Cu(HOO)_2 \cdot 4H_2O$ Associated with the Antiferroelectric Phase Transition. *Ferroelectrics* **2002**, *270*, 375−380.

(79) Okada, K.; Kay, M. I.; Cromer, D. T.; Almodovar, I. Crystal Structure by Neutron Diffraction and Antiferroelectric Phase Transition in Copper Formate Tetrahydrate. *J. Chem. Phys.* **1966**, *44*, 1648−1653.